Drag regimes of circular discs at different inclinations

Sukruth Satheesh, Andreas Spohn, Franck Kerhervé, Laurent Cordier

Drag regimes of circular discs at different inclinations

Sukruth Satheesh[a,*], Andreas Spohn[a], Franck Kerhervé[a], Laurent Cordier[a]

[a]*Département Fluides, Thermique et Combustion, Institut Pprime, UPR 3346 CNRS, ENSMA, Université de Poitiers, 86360 Futuroscope-Chasseneuil, France*

Abstract

Experiments on circular and square plate models were performed in a low-speed water tunnel at a fixed Reynolds number [$O(10^4)$] for inclinations between 0° and 90° with respect to the flow direction. The experiments focus on drag force evolution and the associated flow structures to predict the drag regimes across the range of inclinations considered. Measurements show that drag increases rapidly with inclination for small angles, while at high angles it being nearly independent of inclination. The change between these drag regimes takes place at an inclination of 54°, with hydrogen bubble and PIV flow visualizations indicating this to be accompanied by a change in the wake flow structure as well. Trailing vortices at low angles suggests the existence of induced drag, while shedding of shear layers from all around model circumference at high angles points to the dominance of pressure drag as in the case of bluff bodies.

Keywords: Drag force, PIV, inclination, Cross-flow disc, bluff body wake

1. Introduction

Understanding the drag behaviour of thin flat plates and cylinders in cross-flow is one of the fundamental problems of interest in fluid dynamics, and has been studied for a long time using theory, numerics, and experiments. It is a problem rich in physics, involving several flow phenomena including wake transition which are dependent on Reynolds number (Re, ratio of inertial force to viscous force, based on characteristic body length), along with other conditions such as orientation, geometry, amongst others. The dependency of forces, motion and wake

*Corresponding author
Email address: sukruth.satheesh@univ-poitiers.fr (Sukruth Satheesh)

transitions on Re, fineness ratio (χ, ratio of disc diameter to thickness) and inclination are even more important in the case of flat circular plates in cross-flow. While flow around freely falling discs has been studied both experimentally and numerically at low Reynolds numbers [$O(10^2)$] ([1, 2, 3] and others), studies of low aspect ratio flat plates in a cross-flow with inclinations varying between 0° and 90° at these intermediate Re remain scarce. The goal of this study is to better understand the synergy of various drag contributing physical mechanisms, and for improving the design of many engineering systems. These range from their potential use in Autonomous Underwater and Micro Aerial Vehicles (AUV's, MAV's) for control surfaces and wings, marine structures to energy harvesters or even ground-based structures such as billboards, solar panels and floodlights wherein the operational Re is intermediate [$O(10^3 - 10^5)$].

Fail et al. [4] conducted one of the earliest set of experiments on understanding the effect of plate geometry on drag forces in cross-flow. They found the generated wake to be not dependent on the plate profile, especially for axisymmetric bodies. Calvert [5] performed experiments involving pressure and wake velocity measurements on circular discs with fineness ratio of 32 and $Re = (3.5 - 5) \times 10^4$ at different inclinations, and found that the vortex shedding frequency increases with disc inclination (angle measured w.r.t disc normal), and that the plane of vortex shedding is not fixed but varies azimuthally with time when the disc face is perpendicular to the flow. This latter finding has also been verified and explained in detail using hot-wire measurements and dye-flow and laser-induced fluorescence snapshots by Miau et al. [6]. Torres and Mueller [7] have performed experiments over different wing planforms at aspect ratios (AR, ratio of square of wingspan to the wing area) for MAV applications. They observed very high lift forces and stall angles in $AR \leqslant 1.5$ planforms, and a drop in drag after wing stall even as the angle of attack (AOA, measured as the angle subtended by the model and flow direction) increases. But this feature has not been explored further. Shields and Mohseni [8] have performed a series of experiments to study the effect of side-slip on flat plates of different aspect ratios and configurations, over a range of Reynolds numbers ($Re = (5 - 10) \times 10^4$) and AOA. The reduction in drag after stall for low AR plates is attributed to the post-stall detachment of the trailing vortices leading to a drop in induced drag. Although the force measurements have been corrected for blockage, it is not clear if the very high blockage in these cases also affect the stall angle and drag reduction. DeVoria and Mohseni

[9] have conducted force and flow visualization experiments on low AR rectangular plates at $Re = 8 \times 10^4$ over a range of inclinations, and report sustained high lift generation with inclination occurring only in models of $AR < 1.5$ by reattachment of mean-flow due to the downwash of tip vortex. It is also indicated that the closer tip vortices occurring in low AR plates delays the flow reattachment point on the trailing edge compared to that observed on high AR plates.

In terms of AOA (denoted by α), available literature focuses mostly on lift and drag forces of non-circular plates ranging from 0° to 45°. To our best knowledge, investigations covering details of flow in the entire range of inclinations ($45° \leqslant \alpha < 90°$ in particular) remain scarce. Chen and Fang [10] conducted a series of experiments to study the vortex shedding characteristics of wall-to-wall mounted flat plates ($\chi = 1 - 10$) at several α, Reynolds numbers and plate chamfer angle, and mention that chamfer angle has a stronger effect on the shedding phenomena than Re due to the shift of flow separation point along the chamfer direction (from the front edge to rear edge for reducing α). This shift was found to be dependent on the inclination especially for cases $\alpha \leqslant 40°$. Earlier studies [4] have identified minimal effect of geometry in low AR, high Re scenarios. However, it has been reported by a few works [8, 9, 11, 12] that drag force has a weak dependence on Reynolds number over a specific range of low aspect ratios ($0.75 \leqslant AR \leqslant 1.33$) at $\alpha = 90°$. For inclined circular plates, neither is it completely clear if the same dependency holds, nor is the flow physics behind the post-stall drag behaviour well established. With flat plates aligned with the flow direction, skin-friction drag dominates over the pressure drag component, whereas in cross-flow plates, it is the opposite. They thus behave as so-called bluff bodies. Over the intermediate angles, both pressure drag and skin-friction drag exist alongside induced drag. It is not known if there exists or even what constitutes the limiting angle for a body to be deemed bluff. Former studies have not identified the demarcation between these regimes. This work focuses on identifying the inclinations at which this transition of drag regimes occur. In discs, the origin of trailing vortices is not imposed by the plate geometry whereas in square plates the formation of trailing vortices along the lateral sides is imposed. The aim of this work is on understanding and tackling these questions by correlating the forces generated by discs over a range of inclinations to the wake characteristics, and comparing them with that presented by square plates of equal area operating at same conditions.

The paper is organized as follows. Section 2 describes the experimental setup and the utilized instrumentation. Force measurements and flow visualization results are presented in section 3, finally ending with an overarching discussion in section 4 that correlates forces to the visualizations and details the underlying drag regimes at different angles of attack.

2. Experimental Setup

Experiments were conducted in a low-speed water tunnel to facilitate the combination of force measurements, PIV and flow visualization. Figure 1 shows a schematic of the test section and model arrangement. The overall test section is 2.1 m long and 0.51× 0.33 m^2 in cross-section, the freestream velocity (U_∞) ranging from 0.05 to 0.45 ms^{-1}. Optically transparent circular disc models of diameter (d) 0.11 m and thickness (t) 2.2 mm were fabricated from polycarbonate, ensuring the fineness ratio ($\chi = 50$) is similar to that observed in literature. Model edges were chamfered by 60° in order to fix the flow separation locations and minimize the effect of flow reattachment on the generated forces. The model was mounted in the tunnel such that is equidistant from all the boundaries, and connected to a force sensor located outside via carbon fibre sting. Interference effects was minimized by ensuring that the horizontal strut length of the sting was greater than $2d$. The disc inclination is measured as the angle subtended by the disc surface with flow direction (α), as highlighted in figure 1. Therefore, $\alpha = 90°$ corresponds to the case when disc face is normal to the flow, while $\alpha = 0°$ to when the disc face is along flow direction. In this work, AOA and inclination correspond to the same variable and are used interchangeably. With disc inclination being the primary variable of interest, and to reduce model swap during experimentation, a hinge-based mechanism was developed in order to continuously vary the disc inclination in steps of 10°. Comparison with less invasive fixed angle model mounts were also conducted in order to assure that the hinge mechanism did not affect the force measurements. The blockage ratio, computed as the ratio of disc area to the water tunnel cross-sectional area was around 5.5% when $\alpha = 90°$, and reduces with reducing α. The hinge/pivot arm length of the mechanism was very small [O(1 mm)], ensuring that the change in gap between model and boundaries do not influence the drag measurements. Square plates with exposed area equal to that of discs were similarly fabricated and tested.

A single component piezoelectric load-cell with a resolution of 0.002 N and peak load capacity of 10 N was utilized to measure the total drag. Calibration using known weights was performed to achieve a high load resolution. Particle Image Velocimetry (PIV) [13] was undertaken to visualize the flow quantitatively. A 532 nm green continuous wave laser and equipped with ancillary optics was used to generate a planar laser sheet and aligned onto the inclined disc for wake visualization. A 2048×2048 pixels resolution high speed camera with a f/1.2 12.5-75 mm focal length lens and neutrally buoyant seeding particles of 20 μm diameter was used for experiments. The laser sheet was horizontal and imaging undertaken through a mirror mounted underneath the tunnel at 45°, the image acquisition rate being 80 fps. The captured images were processed by intensity thresholding with the non-illuminated regions masked. PIV analysis was done iteratively using multi-pass technique, the starting and final interrogation window sizes being 128×128 and 54×54 pixels respectively, and overlap of 50% to yield 4575 vectors in each velocity field, covering approximately a field of view of around 36.86×36.86 cm. The outlier vectors obtained from the cross-correlation scheme were identified after applying a threshold and replaced with new values obtained from averaging the vectors neighbouring the outlier. Hydrogen bubble [14] sheet was generated in the horizontal plane located approximately mid-body to visualize the wake evolution. A 50 μm stainless steel wire mounted taut between 2 supports is used as cathode– source of hydrogen bubbles when supplied with a voltage of 80 V from a regulated power supply. The wire was located just upstream of the model and in contact with its leading edge in order to seed the flow, especially the model base region. Pulsed or continuous bubble sheets can be generated using a computer-controlled electronic switch which enable time lines to be marked outside the central recirculation region of the wake.

3. Results

The circular disc was mounted within the water tunnel such that the disc normal is in the middle of test section, thus ensuring that the model was equidistant to the tunnel walls and the free surface. With the expected disc drag forces at this Re being very low [$O(10^{-1})\ N$], the effect of noise and drift would be significant and is essential to minimize their effect. Thus, the force data from the piezoelectric sensor was sampled at 5 kHz, and the measured signal filtered and compensated for

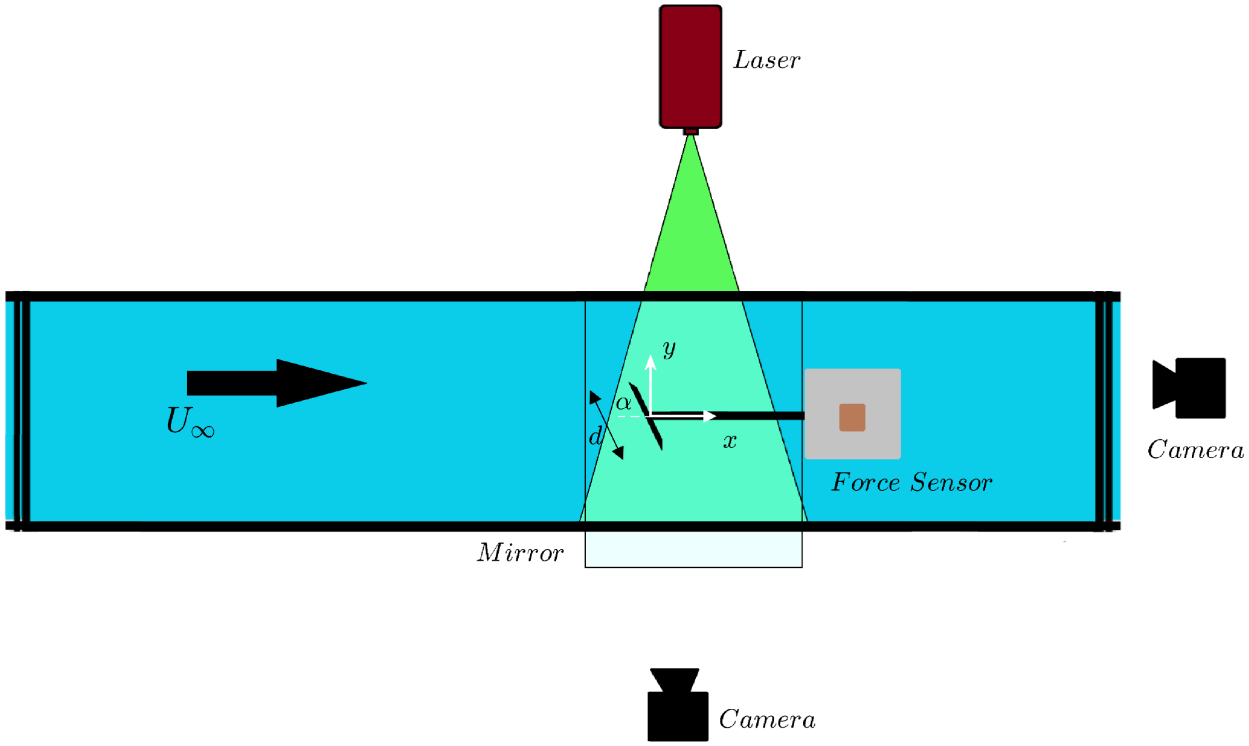

Figure 1: Top view of the experimental setup

drift. The drag generated only by the sting was subtracted from the total drag in order to calculate the model drag. The filtered drag signal was averaged (F) and non-dimensionalized using dynamic pressure and the maximum exposed disc area (A, at $\alpha = 90°$), as seen in equation 1 to obtain the drag coefficient (C_D) with ρ being fluid density. The data was acquired for 180 seconds at each inclination, the acquisition undertaken after flow unsteadiness due to model rotation is minimized.

$$C_D = \frac{F}{\frac{1}{2}\rho U_\infty^2 \cdot A} \tag{1}$$

Reynolds number ($Re_d = U_\infty d/\nu$) is calculated with disc diameter as the characteristic length and ν the kinematic viscosity of water, is fixed at 1×10^4.

3.1. Effect of inclination on drag force

Figure 2 presents the variation of drag coefficient for disc and square plate as a function of inclination, the y-axis plotted in logarithmic scale to highlight the change in order of magnitude of drag coefficient. By using a fixed value of exposed disc area for non-dimensionalization, the trend

of drag coefficient with inclination is in essence that of the drag force. This plot indicates that C_D (plotted as ● and ■, for disc and square plate, respectively) is nearly constant at ~ 1.3 over a small range of inclinations ($\alpha \sim 70^\circ - 90^\circ$). However, the reduction in C_D with decreasing α is rapid post 30°, reaching a value of $\simeq 0.015$ at $\alpha = 0^\circ$. The near similar C_D trends for disc and square plate indicates the model geometry to have negligible bearing on the drag forces.

With discs and square plates being canonical structures, a significant number of studies have been performed over the years spanning a wide range of Reynolds numbers, blockage ratios, model fineness ratios and other test conditions. For the sake of brevity, only a few results from literature have been plotted here. The current measurements are in good agreement with those of Satheesh and Huera-Huarte [12] and Maskell [15] for square plates and discs, respectively in cross-flow. Results by Blevins [16] for a plate aligned with the flow ($\alpha = 0^\circ$) have also been plotted here only for the sake of completeness, and are very close to the obtained results. This confirms the capability of force sensor to measure very low force magnitudes [$O(10^{-1})$ N]. The work of DeVoria and Mohseni [9] involving lift and drag measurements for square plates over $\alpha = 0^\circ - 45^\circ$ at Reynolds number of $8{\times}10^4$ has also been included in the same plot. It can be seen that our results are in good agreement over most of the inclinations. Hoerner [17] presents an empirical formulation for drag coefficient– $C_D = 1.17 \cdot \sin(\alpha)$, indicating its origins to be from sailing and applicable at $\alpha \geqslant 45^\circ$. This equation seems to have been updated by incorporating more results by NASA [18], indicated as $C_D = 1.28 \cdot \sin(\alpha)$, and has been used in the figure. It can be observed that there is a very good match for $40^\circ \leqslant \alpha \leqslant 90^\circ$, both discs and square plates.

In order to account for the change in blockage with model inclination and the consequent wake realignment, correction technique developed by Gould [19] for plates in cross flow has been implemented, given by equation 2. According to this equation, the corrected drag coefficient(C_{D_c}) is given as a function of measured drag coefficient (C_D) and blockage ratio (B), which in turn depends on the models' projected area in streamwise direction.

$$C_{D_c} = 1.163 \cdot [1 + 2.81 \cdot (C_D \cdot B) - 0.96 \cdot (C_D \cdot B)^2] \tag{2}$$

The model projected area is directly related to its inclination $0.25\pi(d \sin\alpha)^2$ and $(a \sin\alpha)^2$,

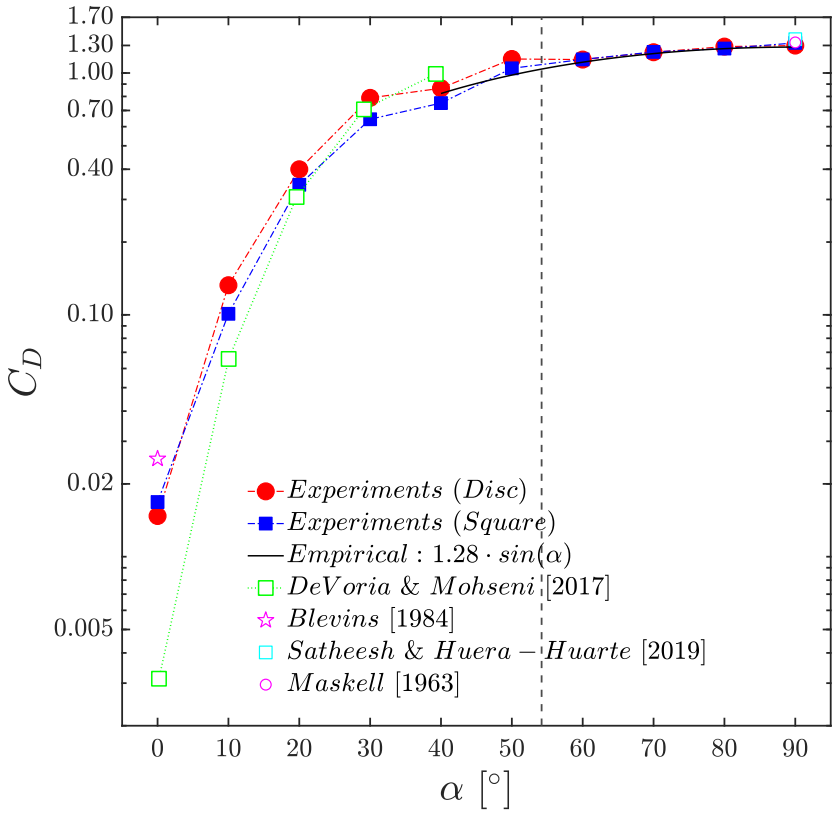

Figure 2: Variation of measured drag coefficient with inclination for disc and square plate. Dashed vertical line marks the critical angle of transition between the induced and pressure drag dominated regimes.

for discs and square plates respectively. Thus, the projected area is maximum when $\alpha = 90°$ and reduces with α. Figure 3a presents the variation of corrected drag coefficient with inclination, showing a high correlation coefficient ($C_{D_c} = -0.01572\alpha^2 + 0.06443\alpha + 1.344, R^2 = 0.996$). It can be observed that C_{D_c} increases in almost a linear manner with increasing α, but the rate of increase in drag is significantly lowered once α is over 60°. To corroborate this, the empirical drag formulation along with the projected area relation (for B calculation) was substituted into equation 2, generating a trigonometric relation given by–

$$C_{D_c} = 1.163 + 0.2399 \cdot \sin^3(\alpha) - 0.006 \cdot \sin^6(\alpha) \tag{3}$$

To identify the change in trend/curvature of the drag plot, the inflection point is calculated for equation 3 using the $\partial^2 C_{D_c}/\partial\alpha^2 = 0$ relation, yielding $\alpha_{crit} = 54.2°$. This has been plotted as

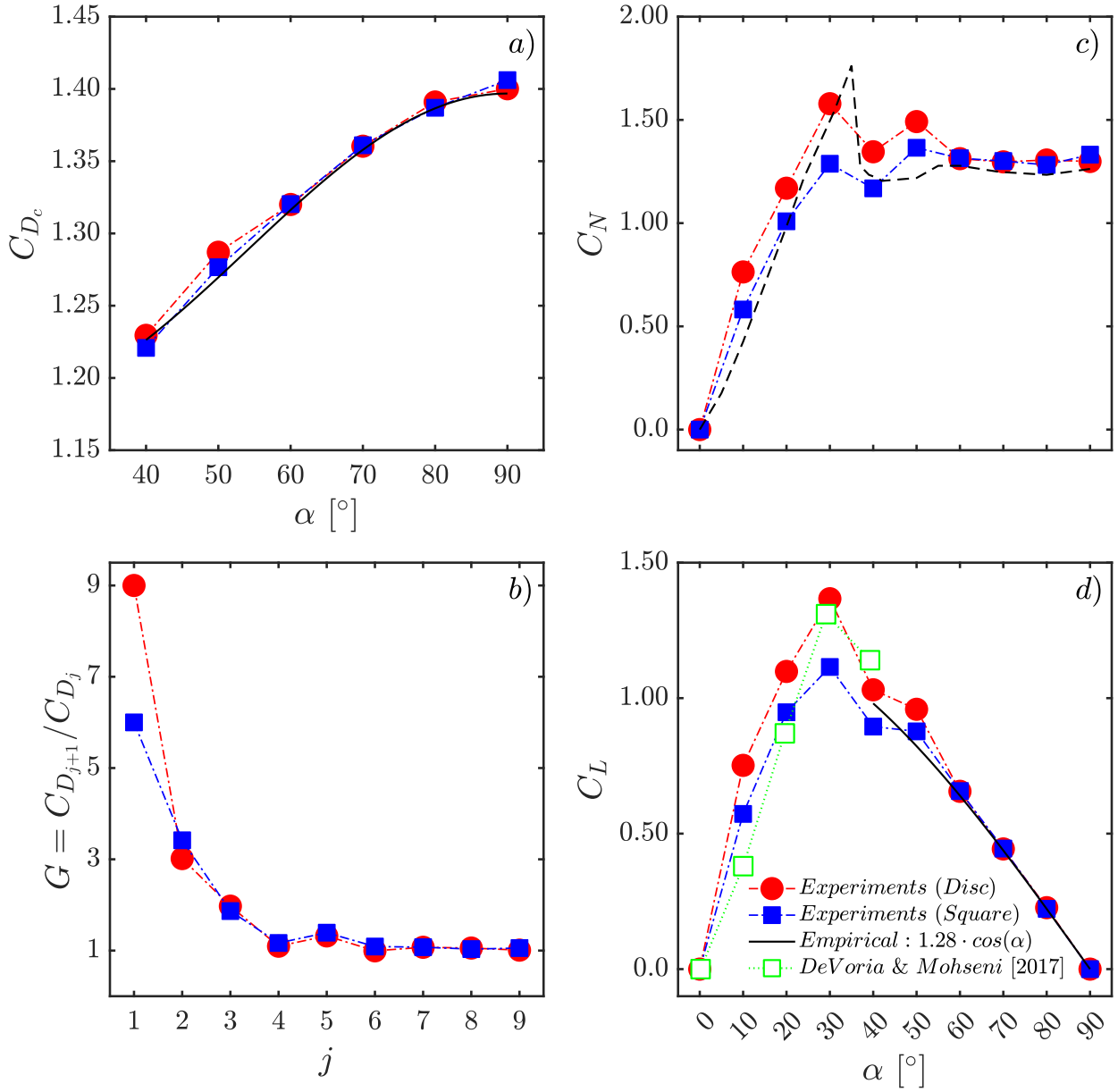

Figure 3: Variation of (a) corrected drag coefficient, (b) drag gain, (c) normal force coefficient, and (d) lift coefficient with inclination

a dashed vertical line in figure 2. This information, obtained purely from empirical drag relation and current model/test section dimensions explicitly validates the aforementioned observations– that the gain in drag coefficient ($G = C_{D_{j+1}}/C_{D_j}$) with inclination reduces after α_{crit} to a value around 1. This can also be seen in figure 3b where G remains nearly constant after $j = 6$

$(C_{D_{60}}/C_{D_{50}})$, implying that drag coefficient is nearly independent of inclination. To reinforce the observations regarding α_{crit}, curve-fitting using a quartic polynomial ($C_{D_{circ}} = 0.08368\alpha^4 - 0.02684\alpha^3 - 0.3507\alpha^2 + 0.5024\alpha + 1.024$, $R^2 = 0.99$; $C_{D_{sq}} = 0.07636\alpha^4 - 0.05447\alpha^3 - 0.2915\alpha^2 + 0.5658\alpha + 0.9431$, $R^2 = 0.99$) was employed on the current experimental data over the entire range of inclinations. On solving the expressions for inflection point, the resulting critical angle for discs and squares are very close to that obtained from the empirical relation.

For inclined thin flat plates in a flow, the suction peak does not exist on the plate surface. Therefore, the contribution of axial force component on lift and drag is small and can be neglected. This assumption allows utilizing the C_D and α information to estimate normal force ($C_N \approx C_D/\sin\alpha$) and lift force ($C_L \approx C_N \cos\alpha$) coefficients, which have been plotted in figures 3c and 3d respectively. The results in figure 3c clearly highlight the rapid rise in C_N with α followed by an abrupt drop to a value of ~ 1.3, the drop occurring around 40°. Similarly, figure 3d presents lift curves for discs and squares. At high inclination ($\alpha \rightarrow 90°$), the data for squares and discs match very well with the empirical formulation ($C_L = 1.28 \cdot \cos\alpha$), deviating only when $\alpha < 60°$. This confirms the assumption of very low axial force magnitudes. At low α, the trends are in line with results of DeVoria and Mohseni [9] for squares. Even though exact magnitudes of C_N and C_L are not obtained through this method, they capture the trends extremely well, especially the stall location in lift curve.

3.2. Flow visualization

PIV and hydrogen-bubble flow visualizations were undertaken at specific inclinations in the near wake to analyze in greater detail the transition process observed in force measurements. The 2D-2C PIV results are time averaged in order to describe the mean-flow characteristics at each inclination. The time window (Δt) of 0.25 s for averaging was selected after analyzing the results over several other window sizes, with this window size providing a balance between the observable flow structures and their magnitude comparable to that presented in literature [9, 11, 12].

Figure 4 presents a montage of instantaneous hydrogen bubble and time-averaged PIV results (xy plane). Vorticity (ω_z) obtained through PIV has been quantified based on the coordinate axes setup, with clockwise rotation being negative and counter-clockwise positive, denoted by

red and blue respectively in the colormap, and non-dimensionalized using disc diameter and the flow velocity. Each row corresponds to a specific inclination, the first column presenting the instantaneous hydrogen bubble snapshots and the second column vorticity from PIV. The plots have been arranged in decreasing inclination, starting from the cross-flow condition ($\alpha = 90°$) to $\alpha = 30°$ case, the lowest inclination of interest in this scenario. Figures 4a and 4b present flow separation from the edges and visible wake evolution, which is highly symmetric. The measured vorticity extends approximately two disc diameters downstream. Figure 4a shows the various Kelvin-Helmholtz (K-H) vortices that are generated by instabilities in the separated flow which appear as extended shear layers in figure 4b. At $\alpha = 60°$ (figures 4c, 4d), differences in the separated flow from the leading (LE) and trailing (TE) edges are clearly noticeable, with separated flow from the LE presenting K-H vortices and extending $1.75d$ downstream as before, while that from TE being smaller ($1.5d$). In figures 4e and 4f, the LE separated flow appears to be similar as before but with higher deflection compared to the former cases, resulting in increased proximity of the shear layer to the disc base region. Meanwhile at TE, a vortex evolves and traverses downstream, which appears to be fixed/pinned at $x \sim 0.5d$ in the time-averaged snapshot, unlike the observations in previous inclinations. At $\alpha = 40°$ (figures 4g, 4h), the recirculating flow from LE is in close proximity to the disc base while the TE vortex appears to be pinned as in figure 4f, but is not prominent. Finally, at $\alpha = 30°$ (figures 4i, 4j), the recirculating flow from LE completely envelops the disc and flow exits smoothly from TE with no vortex formation.

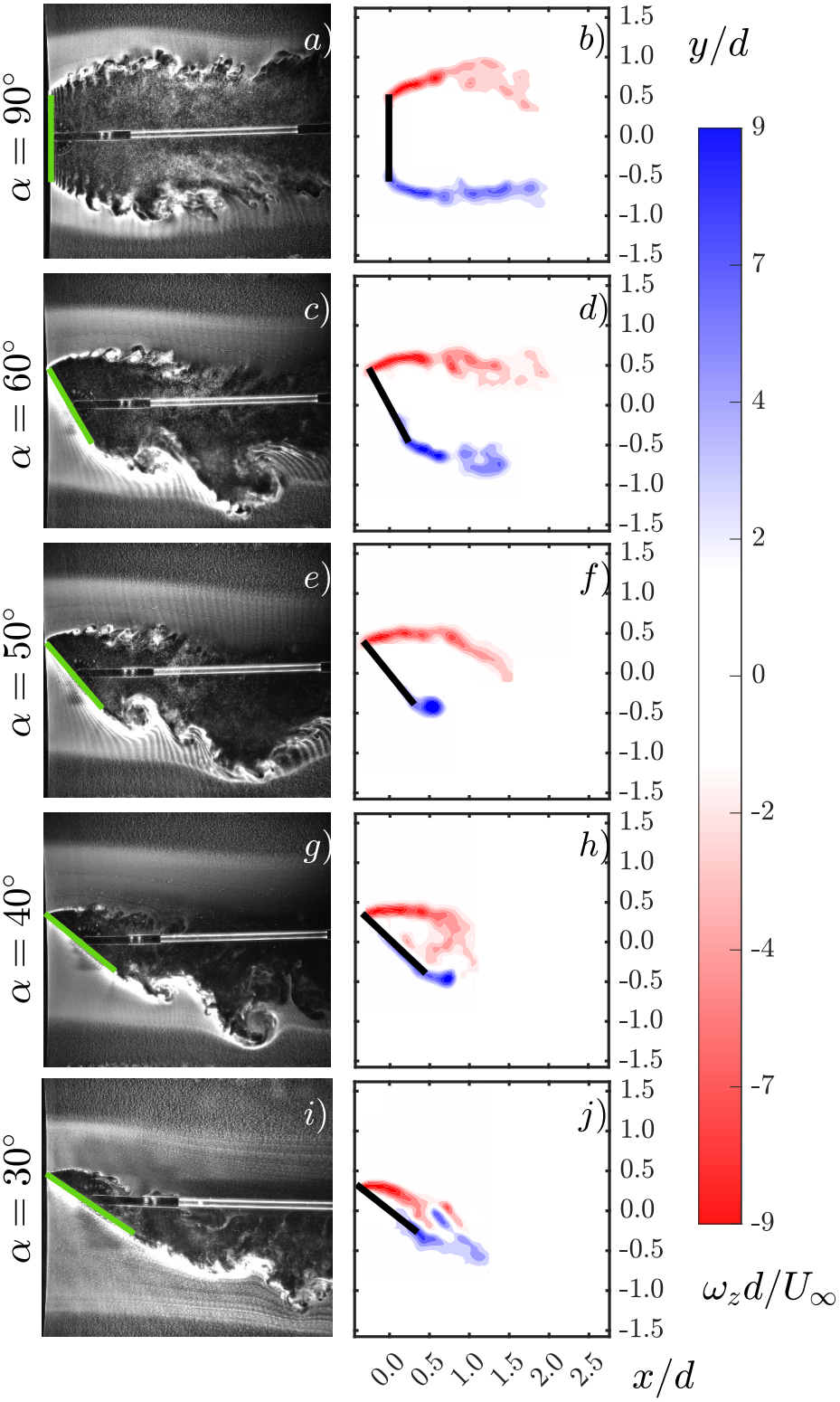

Figure 4: Instantaneous hydrogen bubble and PIV disc flow visualizations at different inclinations

These results precisely indicate the various flow structures existing on discs at different inclinations. The plots at $\alpha = 90°$ is as expected involving symmetric separated flows with minimal differences in non-dimensional vorticities as well. This has been observed by several other researchers in different geometries ranging from discs, squares to even elliptical and rectangular plates ([12, 11, 20], amongst several others) in cross-flow. The plots for α of 40° and 30° are completely in line with those obtained by DeVoria and Mohseni [9] for square plates, validating the absence of TE vortex at the lowest visualized inclination, and the current flow visualization setup. Similarly, the flow structures observed by Linehan and Mohseni [21] for square plates' LE and TE at α of 30° and 40° without sideslip matches well with the current observations.

Even though figure 4 highlights the specific flow structures at α of 60° and 50° that have not been observed in literature till now, circulation ($\Gamma = \iint \omega_z \cdot ndS$) has also been evaluated to complement the observations. Figure 5 presents the evolution of LE and TE circulation over inclinations of interest. Time-averaged circulation values in the regions about LE and TE are represented by ▲ and ▼ respectively, and non-dimensionalized using the disc diameter and flow velocity. Based on the sign convention, LE circulation values are negative but have been presented in the same plot to enhance ease of comparison with the corresponding values at TE. The plot indicates that the TE circulation monotonically decreases with decreasing α, starting from a value of approximately 4 and ending at nearly 0. Meanwhile, the LE circulation also starts at a value of around 4 as expected at $\alpha = 90°$, and decreases with α before presenting a distinct step in circulation at $\alpha = 50°$ to reaching a final value of approximately 1.2 at the minimum inclination visualized here. LE and TE circulation values from DeVoria and Mohseni [9] for square plates at $\alpha \leqslant 45°$ have also been included in the same plot (non-dimensionalized using effective diameter instead of chord as in their work), and it can be seen that their magnitudes and trends are well in agreement with the current measurements.

Finally, time-averaged hydrogen bubble visualizations have been performed for both discs and squares in the near wake to visualize the flow structures emanating from the lateral edges. This is to verify that the observed changes in circulation can indeed be attributed to the differences observed in the drag force. To visualize yz plane, a vertical laser sheet was generated at $x = d/2$ downstream of the model. This visualization angle aligns the flow direction to be outward from

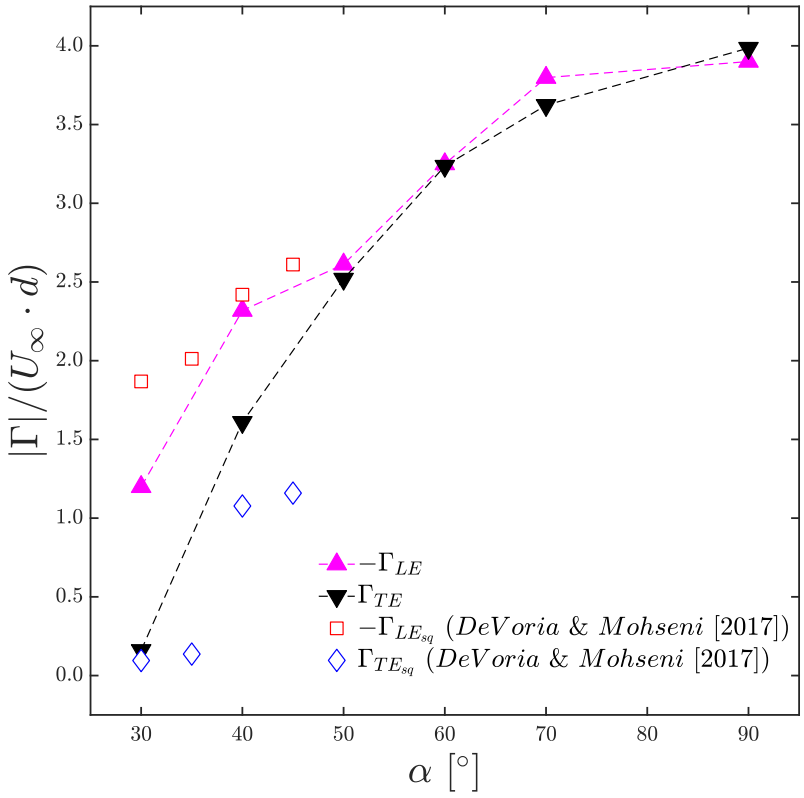

Figure 5: Variation of Leading Edge and Trailing Edge non-dimensional circulation for discs with inclination

the plane. The central white region highlights the model support. The model's axis of inclination is vertical. Model LE exists to right of the support and TE to the left, emphasized by red and blue outlines respectively. Figure 6 presents this scenario for specific inclinations. Sectors of higher light intensity indicate regions wherein flow is steady, while the diffuse ones are regions of increased skewing and/or flow unsteadiness. A horizontal hydrogen bubble sheet was generated upstream of the model and closer to the lateral edge, which appears as intense bright horizontal sectors located on either side of the model cutting across the vertical laser sheet in all the averaged images.

From figures 6a and 6b ($\alpha = 90°$), the near wake for discs and squares are remarkably similar and symmetric about the central support. This indicates that the flow separation process is blind to the location of edge in this condition. At $\alpha = 60°$, a bright sector exists downstream and below the model that corresponds to the flow from the lateral edge, with diffuse regions occurring in the direction towards LE. Figure 6c also shows that the separated flow for disc is more curved than to

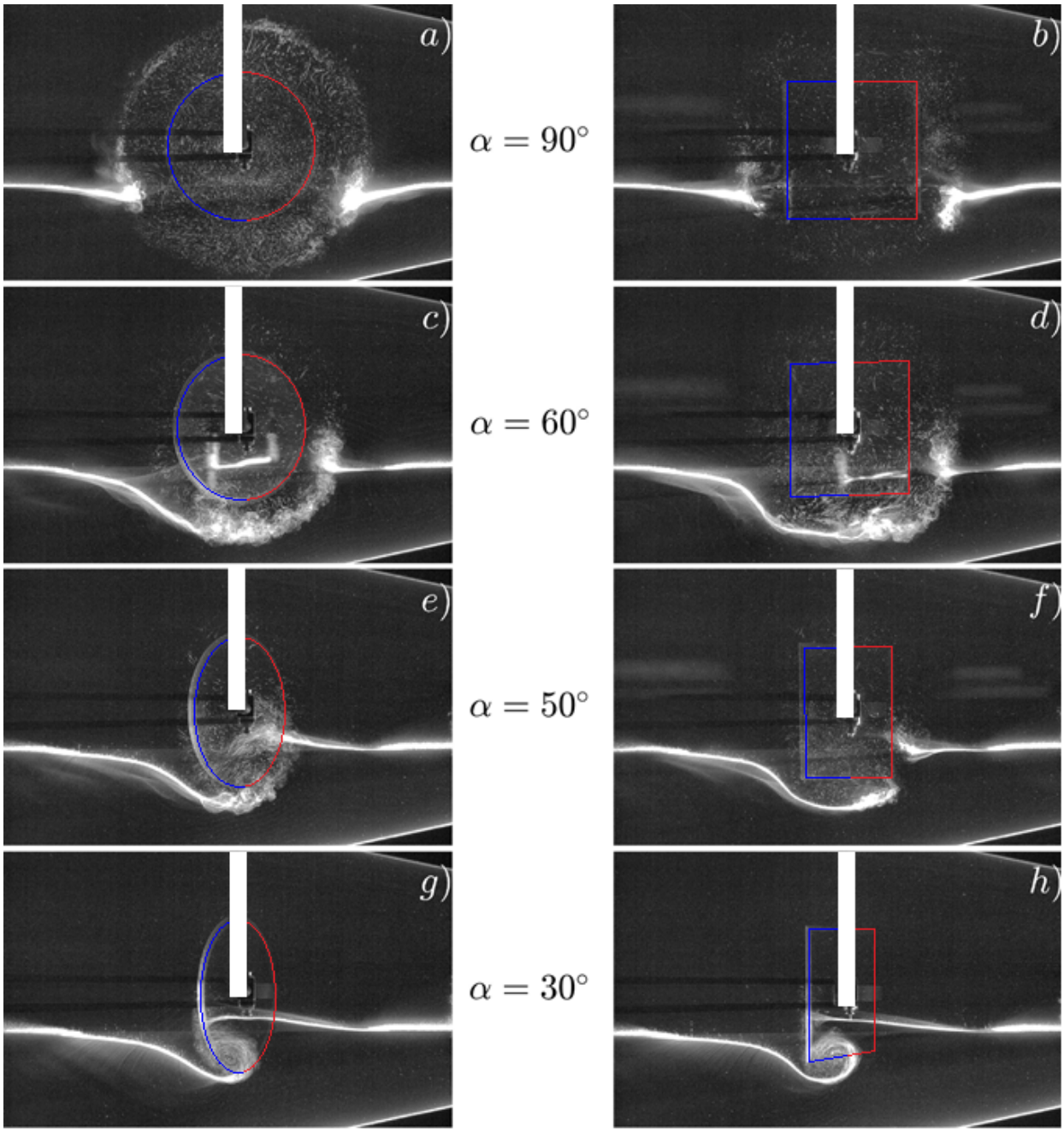

Figure 6: Time-averaged hydrogen bubble flow visualizations of lateral edge in near wake at different inclinations for discs and squares. Model LE (red) and TE (blue) is to the right and left of central support, respectively.

that in 6d for squares, the flow following more closely the model geometry. Further decrease in inclination (figures 6e, 6f) results in an increase in the length of steady flow region closer to the TE, while increasing their curvature as well. Finally at $\alpha = 30°$ (figures 6g, 6h), the bubble sheet has

no significant distortion and presents a prominent vortex emanating from the lateral edge (wing-tip vortex), located approximately below the vertical support for both discs and squares. The size of wing-tip vortex is also significant and extends approximately 25-30% of the model diameter at this downstream location. There also exists a bright horizontal sector above the vortex highlighting the extent of the recirculating bubble that exists on the model base region, which was also observed in PIV. In all, consolidating the circulation results from figure 5 and lateral flow visualizations of figure 6 presents a comprehensive picture of the flow around discs. At $\alpha = 90°$, the symmetric flow condition implies circulation magnitudes to be near similar as well. With reducing inclination, the LE and TE circulation values diminish, while wing-tip vortices which are manifestations of a lifting surface ($\alpha = 30°$) increase in prominence.

4. Discussion and final remarks

The results from drag force measurements and flow visualization have provided a detailed view regarding the drag regimes and their associated flow structures. The force measurements indicated that the changes in C_D magnitudes are almost negligible at high inclinations ($\alpha \sim 60° - 90°$), below which the drop in drag values is rapid. Although the work by Gould [19] is developed for cross-flow plates mounted centrally or in close proximity to a wind tunnel wall and specific test conditions ($0 < C_D \cdot B \leqslant 0.3$), the current work highlights that this correction technique is applicable for inclined models as well. However, it must be observed that there exists a range of inclinations over which this correction technique is valid, namely $45° \leqslant \alpha \leqslant 90°$. At lower inclinations the drag coefficient predicted by this equation is not comparable to the measured values. Using the empirical formulations ([17, 18]) turned out to be more accurate for comparing the current drag measurements, for they are independent of model geometry and developed for plates of finite aspect ratio. The visualizations elucidate reason for the observed drag behaviour– the reorganization process occurring between α of 60° and 50° of the separated flow from LE to a recirculating flow in close proximity to the disc base, and the separated flow from TE to a slow vortex shedding process that appears as a pinned vortex in PIV. This transition process is not dependent on plate geometry. Some of the flow structures observed by Gao et al. [22], Zhao et al. [23] in their numerical studies on discs and squares at $Re = 300$ and different inclinations are similar to that

observed here experimentally, indicating the effect of Re to be not very significant on flow physics even though Re magnitudes are vastly different. However, changes in plate aspect ratio or Re may have certain effects on α_{crit} owing to the change in strength and proximity of wing-tip vortices to the mean-flow, and is beyond the scope of this work.

The current work in fact presents a potential origin for the empirical formulations– the aspect of minimal effect of axial force on lift and drag due to the non-existence of the suction peak on inclined thin plates. Besides, even by using the C_L, C_D results of DeVoria and Mohseni [9] to perform an order of magnitude estimation of the induced drag ($C_{D_i} \sim (C_L)^2/\pi$, for square plates) yields that the contribution of induced drag to the total drag (C_{D_i}/C_D, assuming the effect of wing efficiency factor e to be not relevant for calculating this ratio) is dominant only for $0^\circ \leqslant \alpha \leqslant 40^\circ$, after which it drops precipitously. This, along with the knowledge of skin-friction and pressure drag components being the dominant contributors to total drag at $\alpha = 0^\circ$ and $\alpha = 90^\circ$ respectively, reveals the various drag regimes. As α increases from 0°, the low AR plates function as lifting surfaces. Thus, the contribution of induced drag to the total drag increases which peaks around 40°, and is mainly due to vortical wake generated by lift. Further increase in α results in lift reduction due to stall, consequently reducing the induced drag. In the second regime ($\alpha > 50^\circ$), drag is nearly independent of inclination. The slow drag evolution in this regime is well described by the empirical laws given by Hoerner [17] and NASA [18]. Flow visualizations confirm the absence of strong trailing vortices in this regime, suggesting that flow separation across the disc circumference leads to recirculation zone formation with low base pressure. The transition region between the flow regimes dominated by lift and flow separation ($40^\circ \leqslant \alpha \leqslant 60^\circ$) is marked by the development of a vortex shedding process from the trailing edge and the absence of wing-tip vortices. At the same time the difference in circulation magnitudes shed from leading and trailing edges reduces. This points to lift reduction while total drag continues to rise, implying that the contribution of pressure drag increases. In all, the current experiments highlight the various flow regimes and expound the transition process. At α of 90°, the separated flow is symmetric, with low base pressure. Flow continues to remain separated from model LE and TE, but with an asymmetry induced by α till around 60°. This regime corresponds to pressure drag. Further reduction in angle of attack results in a change in shedding process, resulting in separated flow from model

LE to approach closer to model base, while a slow vortex shedding is apparent at model TE, with this process occurring till $\alpha = 40°$. Further reduction in α results in separated flow from LE to encapsulate the base region and no flow separation at TE, with strong tip vortices emanating from lateral edges confirming strong lift forces and the consequent induced drag. These observations reaffirm the current results of the bluff body definition being apt for models at inclination greater than 50°.

Acknowledgements

The present work is funded by the French organization ANR under the project COWAVE ANR-17-CE22-0008.

References

[1] S. B. Field, M. Klaus, M. G. Moore, F. Nori, Chaotic dynamics of falling disks, Nature 388 (6639) (1997) 252–254.

[2] P. Ern, F. Risso, D. Fabre, J. Magnaudet, Wake-induced oscillatory paths of bodies freely rising or falling in fluids, Annual Review of Fluid Mechanics 44 (2012) 97–121.

[3] X. Tian, Z. Hu, H. Lu, J. Yang, Direct numerical simulations on the flow past an inclined circular disk, Journal of Fluids and Structures 72 (2017) 152–168.

[4] R. Fail, J. A. Lawford, R. C. W. Eyre, Low-Speed-Experiments on the Wake Characteristics of Flat Plates normal to an Air Stream, Tech. rep., Aeronautical Research Council R&M 3120 (1959).

[5] J. R. Calvert, Experiments on the flow past an inclined disk, Journal of Fluid Mechanics 29 (4) (1967) 691–703.

[6] J. J. Miau, T. S. Leu, T. W. Liu, J. H. Chou, On vortex shedding behind a circular disk, Experiments in fluids 23 (3) (1997) 225–233.

[7] G. E. Torres, T. J. Mueller, Low-aspect-ratio wing aerodynamics at low Reynolds number, AIAA Journal 42 (5) (2004) 865–873.

[8] M. Shields, K. Mohseni, Effects of sideslip on the aerodynamics of low-aspect-ratio low-Reynolds-number wings, AIAA journal 50 (1) (2012) 85–99.

[9] A. C. DeVoria, K. Mohseni, On the mechanism of high-incidence lift generation for steadily translating low-aspect-ratio wings, Journal of Fluid Mechanics 813 (2017) 110–126.

[10] J. M. Chen, Y. C. Fang, Strouhal numbers of inclined flat plates, Journal of Wind Engineering and Industrial Aerodynamics 61 (2-3) (1996) 99–112.

[11] J. N. Fernando, D. E. Rival, On vortex evolution in the wake of axisymmetric and non-axisymmetric low-aspect-ratio accelerating plates, Physics of Fluids 28 (1) (2016) 017102.

[12] S. Satheesh, F. J. Huera-Huarte, Effect of free surface on a flat plate translating normal to the flow, Ocean Engineering 171 (2019) 458–468.

[13] C. E. Willert, M. Gharib, Digital particle image velocimetry, Experiments in fluids 10 (4) (1991) 181–193.

[14] F. A. Schraub, S. J. Kline, J. Henry, P. W. Runstadler Jr, A. Littell, Use of hydrogen bubbles for quantitative determination of time-dependent velocity fields in low-speed water flows, Journal of Basic Engineering.

[15] E. C. Maskell, A theory of the blockage effects on bluff bodies and stalled wings in a closed wind tunnel, Tech. rep., Aeronautical Research Council R&M 3400 (1963).

[16] R. D. Blevins, Applied fluid dynamics handbook, New York.

[17] S. F. Hoerner, Fluid Dynamic Drag, Hoerner Fluid Dynamics, 1965.

[18] https://www.grc.nasa.gov/WWW/k-12/airplane/kiteincl.html, last Updated May 2021.

[19] R. W. F. Gould, Wake Blockage Corrections in a Closed Wind Tunnel for One or Two Wall-Mounted Models Subject to Separated Flow, Tech. rep., Aeronautical Research Council R&M 3649 (1969).

[20] A. Hemmati, D. H. Wood, R. J. Martinuzzi, Effect of side-edge vortices and secondary induced flow on the wake of normal thin flat plates, International Journal of Heat and Fluid Flow 61 (2016) 197–212.

[21] T. Linehan, K. Mohseni, Leading-edge flow reattachment and the lateral static stability of low-aspect-ratio rectangular wings, Physical Review Fluids 2 (11) (2017) 113901.

[22] S. Gao, L. Tao, X. Tian, J. Yang, Flow around an inclined circular disk, Journal of Fluid Mechanics 851 (2018) 687–714.

[23] Y. Zhao, S. Gao, X. Zhang, X. Guo, X. Li, X. Tian, Direct numerical simulations on the flow past a thin square plate, Physics of Fluids 33 (3) (2021) 034128.